Full differential spectroscopy for high-stability vapor cell optical frequency reference

Tenghui Yang [1,2], **Peter Yun** [1,2,✉], **Rodolphe Boudot** [3], **Qiang Hao** [1,2,4], **Wei Liang** [5,6,✉], **and Shougang Zhang**[1,2]

[1]Key Laboratory of Time Reference and Applications, NTSC, Chinese Academy of Science, Xi'an, 710600, China
[2]University of Chinese Academy of Science, Beijing, 100049, China
[3]FEMTO-ST, CNRS, Université Marie et Louis Pasteur, ENSMM, Besançon, France
[4]Center for Quantum Technologies, Nanyang Technological University, Singapore, 639798, Singapore
[5]Key Laboratory of Semiconductor Display Materials and Chips, Suzhou Institute of Nano-Tech and Nano-Bionics, Chinese Academy of Sciences, Suzhou 215123, China
[6]School of Nano-Tech and Nano-Bionics, University of Science and Technology of China, Hefei 230026, China
[✉]e-mail: yunenxue@ntsc.ac.cn; wliang2019@sinano.ac.cn

ABSTRACT

We propose and experimentally demonstrate a spectroscopic method, named full differential spectroscopy, that uses a single laser beam in retroreflected configuration to manipulate atomic dark states in a vapor cell. Conventional Doppler-free spectroscopy often relies on complex setups or limits from Doppler-broaden background. Here we show that by selectively coupling or decoupling the probe's polarization components with the pump-induced dark state, we can simultaneously obtain both Doppler-free electromagnetically induced transparency and absorption. A differential signal, with enhanced Doppler-free amplitude and highly suppressed background and noise, is thus obtained. We systematically characterize how polarization angle and light power affect the resonance and noise properties. Using this approach, we stabilized a laser to a rubidium vapor cell, achieving a fractional frequency stability of 1.2×10^{-13} at 1 s. These results demonstrate a simple, robust route to high-performance optical frequency references and may also benefit quantum sensing or high-resolution spectroscopy.

Introduction

Atomic spectroscopy is the cornerstone of precision measurement science, underpinning advancements in fundamental physics[1], quantum technologies[2] and metrology[3–5]. Among diverse techniques, saturated absorption spectroscopy (SAS)[6] stands as a pivotal method for overcoming Doppler broadening, essential for applications such as laser frequency stabilization[7–12] and optical frequency references[13–15]. Despite its widespread adoption, SAS suffers from a fundamental limitation: the Doppler-free resonance rides atop a substantial Doppler-broadened background, significantly degrading the signal contrast and limiting the signal-to-noise ratio (SNR).

To mitigate this constraint, differential saturated absorption spectroscopy (DSAS) was developed[16–18]. By employing a reference beam to subtract the Doppler background and reject common-mode noise[19], such as laser amplitude modulation (AM) noise[20], DSAS enhances SNR and signal fidelity. However, this approach introduces optical complexity and susceptibility to beam splitter ratio instabilities, as well as spatial nonuniformity of beams within the atomic medium due to wall effects and nonideal cell windows[21]. These inherent limitations constrain the ultimate achievable SNR and complicate the system integration, particularly for field-deployable or chip-scale atomic devices[22].

Single-beam differential methodologies like polarization spectroscopy (PS)[23–25] and Faraday rotation spectroscopy (FRS)[26–28] have garnered substantial interest. These techniques circumvent the need for reference beams by exploiting pump-induced birefringence, generating antisymmetric (typically dispersive) signals through the differential detection of orthogonal probe polarization, inherently suppressing common-mode noise without active modulation. While elegant, these methods often necessitate auxiliary elements (e.g., static magnetic fields for FRS) and precise polarization control for PS[29], adding layers of complexity and potential noise sources. Improved schemes have also been proposed to obtain Lorentz-type signals through single-beam differential detection by polarization-induced incoherent population pumping[30].

Inspired by the coherent control in bichromatic systems, particularly constructive/destructive manipulation of coherent population trapping (CPT) resonances[31,32], we present here a monochromatic light spectroscopic approach based on the coherent manipulation of atomic dark states. Unlike previous works[33,34] that reported electromagnetically induced transparency (EIT) and absorption (EIA) under different polarization configurations, our method uses a single monochromatic laser beam to

concurrently generate phase-correlated, Lorentzian-shaped EIT and EIA signals, subsequently subtracted to provide a Doppler-free signal with enhanced SNR. Here, the innovation lies on the controlled coupling/decoupling between the pump-generated dark state and orthogonal polarization components of the counter-propagating probe beam. While a single beam is used, this coherent interference induces the simultaneous emergence of Doppler-free Lorentzian EIT and EIA resonances in phase opposition, enabling direct generation, via differential detection, of a high-contrast zero-background differential (DIF) signal. We term this approach full differential spectroscopy (FDS).

Compared with SAS and DSAS, the FDS approach offers enhanced SNR through common-mode noise rejection in a simple single-beam retroreflected configuration. Relative to PS and FRS, FDS eliminates the need for precise polarization control[29] or external magnetic fields, while achieving a comparable or better short-term frequency stability. In contrast to bichromatic CPT-based differential schemes or dual-frequency sub-Doppler spectroscopy (DFSDS)[35,36], FDS uses a single monochromatic light source, significantly reducing the system complexity. These comparisons highlight the interest of FDS for the development of a simple-architecture and high-stability vapor-cell optical frequency reference.

This manuscript details theoretical and experimental investigation of FDS using the ^{87}Rb D_1 line, rigorously characterizing spectral signatures (contrast, amplitude, linewidth) and noise performance versus relative polarization angle (θ) and laser power (P_L). Experimental tests confirm fourfold AM noise suppression and tenfold SNR enhancement compared to traditional SAS. Using FDS, we demonstrate, for a single laser, a fractional frequency stability of 1.2×10^{-13} at 1 s, in good agreement with phase noise measurement. These results demonstrate the potential of the FDS approach for the development of high-stability vapor cell optical frequency standards. Beyond frequency control, the FDS method can explore quantum coherent phenomena, contribute to the development of quantum sensors such as magnetometers[37–39] or gyroscopes[40–42], and advance dynamic control in light-matter interactions[43–45].

Methods

Interaction between light and simplified five-level system

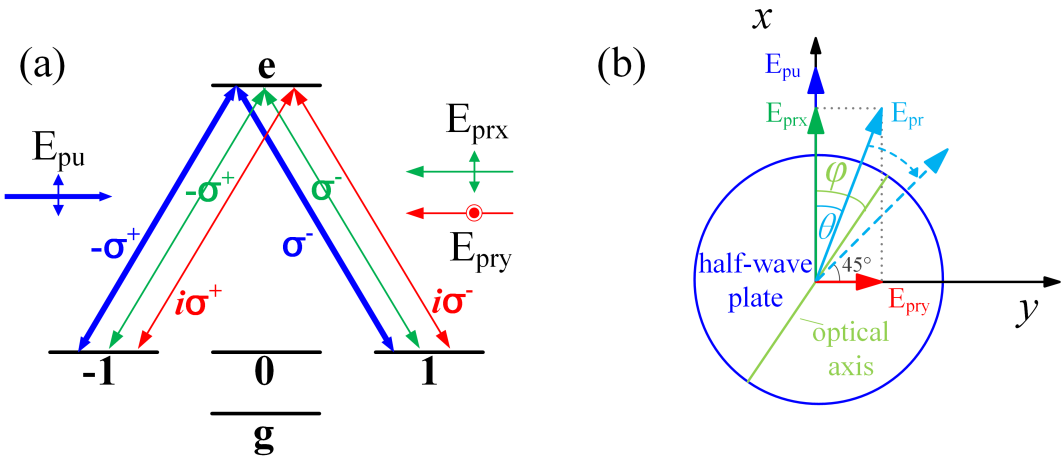


Figure 1. Simplified five-level atomic system and polarization geometry. (a) Simplified five-level atomic system under study, interacting with counter-propagating light beams. *x*- and *y*-axis components of the probe beam are distinguished. (b) Polarization geometry. Representation of the angle between the optical axis of the half-wave plate and *x*-axis, to balance the *x* and *y* direction backgrounds.

Figure 1(a) shows the atom-light interaction system under study. The ground state involved is $\left|5^2S_{1/2}, F = 2\right\rangle$ of ^{87}Rb. The analysis is performed using a simplified five-level atomic system interacting with monochromatic light composed of counterpropagating pump and probe beams, both linearly polarized and originating from the same laser source. The pump polarization aligns with the *x*-axis, while the probe polarization forms an angle θ relative to the *x*-axis (Fig. 1(b)). Their electric fields are denoted as E_{pu} and E_{pr}, respectively. The probe field can be decomposed into components E_{prx} and E_{pry} along the *x*- and *y*-axes, respectively.

Considering the case $I_p < I_{sat}$ (with I_p the pump intensity and I_{sat} the saturation intensity), three competing processes typically arise in the atom-light interaction: (i) Saturation effects, where strong field will gradually deplete the population of the ground state energy levels; (ii) Hyperfine population transfer, where atoms are optically pumped from an initial ground

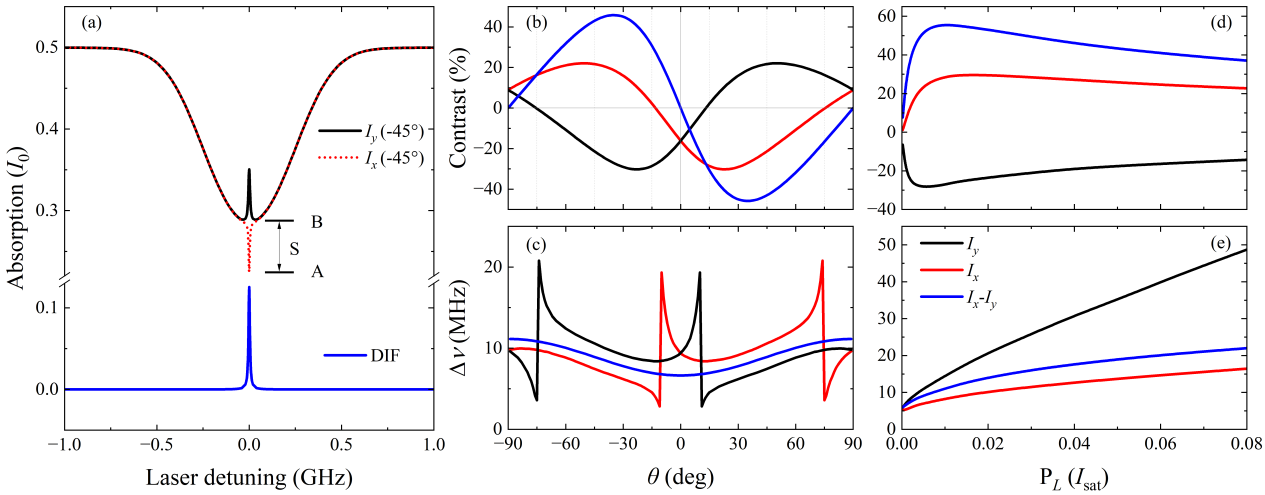


Figure 2. Model-predicted FDS resonance. (a) Calculated EIT (black), EIA (red) and DIF (blue) signals at $\theta = -45°$. Contrast (b) and linewidth $\Delta\nu$ (c) of the sub-Doppler resonance versus the relative polarization angle θ, for a laser power $P_L = 0.0032 I_{sat}$. Contrast (d) and linewidth (e) versus laser power P_L at $\theta = -35°$.

hyperfine level F to an excited state F' and subsequently decay via spontaneous emission into a different ground hyperfine level (e.g., F-1) thereby redistributing populations among the hyperfine ground states; (iii) Zeeman coherence and population redistribution, i.e., optical pumping process that both redistribute populations among ground-state magnetic sub-levels and establish coherent superposition between them. In the case of low pump intensity, Zeeman coherence and population redistribution prevails over both saturation and hyperfine repopulation. Thus, atom-light interaction involves two main processes. First, at null magnetic field, the linearly polarized pump beam, traveling along the quantization axis, can pump atoms into a state superposition of Zeeman sub-levels characterized by their magnetic number m_F. In such a superposition, the differences Δm_F between the participating sub-levels are even (i.e., $\Delta m_F = 0, \pm 2, ...$). These dark states are uncoupled from light (light absorption decrease). In other words, pump beam components (σ^+, σ^-) interact with ground-state Zeeman sub-levels, forming a dark state. Second, probe components ($\parallel$, $\perp$ to pump polarization) decouple/couple with this dark state respectively, generating common dark and bright states. Simultaneous constructive and destructive interference produces EIT and EIA upon detection of the probe's orthogonal polarization components.

The model used in this work shares the same theoretical framework as the one reported in Ref[33]. However, in Ref[33], only numerical solutions for the y-polarized enhanced signal were reported, preventing the prediction of the quantitative evolution of the resonance. In the present work, the analysis is significantly extended by providing analytical steady-state solutions for both the x- and y-polarization components of the probe field. This enables systematic predictions of the resonance characteristics (contrast, linewidth) versus key experimental parameters (polarization angle and laser power) and allows direct comparison with experimental results, a capability absent in Ref[33]. Details are reported in Supplementary Note 1. The latter reports the complete density-matrix derivation, including the explicit Hamiltonian, the Lindblad master equation, the steady-state analytical solutions for the atomic coherence, the velocity-averaged susceptibilities χ_+ and χ_- , and the derivation of I_{xt} and I_{yt}, defined as the x- and y-direction components of the probe transmission after its interaction with the atomic medium. The background levels of I_{xt} and I_{yt} are intrinsically unequal, proportional to $I_0 cos^2\theta$ and $I_0 sin^2\theta$, where I_0 is the intensity of the incident probe beam. To achieve zero-background DIF signals, the polarization of the transmitted probe beam is rotated to exactly 45° using a half-wave plate. The corresponding intensities detected in the x- and y-directions (I_x, I_y) are then expressed by the Jones matrix[46]:

$$\begin{bmatrix} I_x \\ I_y \end{bmatrix} = \begin{bmatrix} cos\varphi^2 - sin\varphi^2 & 2sin\varphi cos\varphi \\ 2sin\varphi cos\varphi & sin\varphi^2 - cos\varphi^2 \end{bmatrix} \begin{bmatrix} I_{xt} \\ I_{yt} \end{bmatrix} \tag{1}$$

where φ is the angle between the half-wave plate's optical axis and the x-axis, as shown in Fig. 1b, given by $\varphi = (45° + \theta)/2$. The balanced detector signals then become:

$$\begin{aligned} I_x &= \left((cos\theta - \sin\theta)\sqrt{I_{xt}} + (cos\theta + \sin\theta)\sqrt{I_{yt}} \right)^2 /2 \\ I_y &= \left((cos\theta + \sin\theta)\sqrt{I_{xt}} - (cos\theta - \sin\theta)\sqrt{I_{yt}} \right)^2 /2 \end{aligned} \tag{2}$$

Theoretically obtained EIT and EIA signals are shown in Fig. 2(a). These signals share identical Doppler-broadened

backgrounds while exhibiting Doppler-free resonances in anti-phase. Their subtraction yields the Doppler-free differential (DIF) signal with doubled amplitude. Figure 2(b) shows the polarization-angle dependence of the sub-Doppler resonance contrast for both transmission signals (I_x, I_y) and the differential signal ($I_x - I_y$). Signal (S) amplitude is defined as the difference between the background (B) and either the absorption (A) valley or peak ($S = B - A$), while the contrast (C) is the ratio of the resonance amplitude to the background ($C = S/B$). Here, positive (negative) values of S or C indicate EIA (EIT). For the DIF signal, the background is the mean of the EIT and EIA backgrounds.

Figure 2(b) reveals that the transmitted signal I_x exhibits EIT from -12° to 75° and EIA elsewhere, while I_y is EIT from -75° to 12° and EIA elsewhere. This phenomenon can be explained as follows: when pump and probe polarization are parallel, constructive interference between their dark states produces enhanced transmission. Conversely, perpendicular polarization induces destructive interference of dark states, yielding enhanced absorption. Competition between these mechanisms governs the intermediate-angle behavior. We note, as in Ref[33], that the maximum contrast does not occur at $\theta = 45^\circ$ due to superposition with saturation effects. The dependence of the calculated linewidth of the EIT, EIA and DIF signals on the relative polarization angle θ is shown in Fig. 2(c). Within the angular range of approximately $10^\circ \leq |\theta| \leq 75^\circ$, the predicted linewidth of the DIF signal lies between those of the EIT and EIA signals. It is consistent with experimental data reported in Fig. 5(c). The calculated contrast and linewidth of EIT, EIA and DIF signals is displayed versus the laser power P_L (at $\theta = -35^\circ$) on Figs. 2(d) and 2(e). The contrast increases rapidly at low powers and saturates at high powers, while the linewidth exhibits clear power broadening. These theoretical predictions serve as the basis for experimental characterizations presented in Fig. 5. The good qualitative agreement between theory and experiment validates the underlying physical model.

Experimental setup

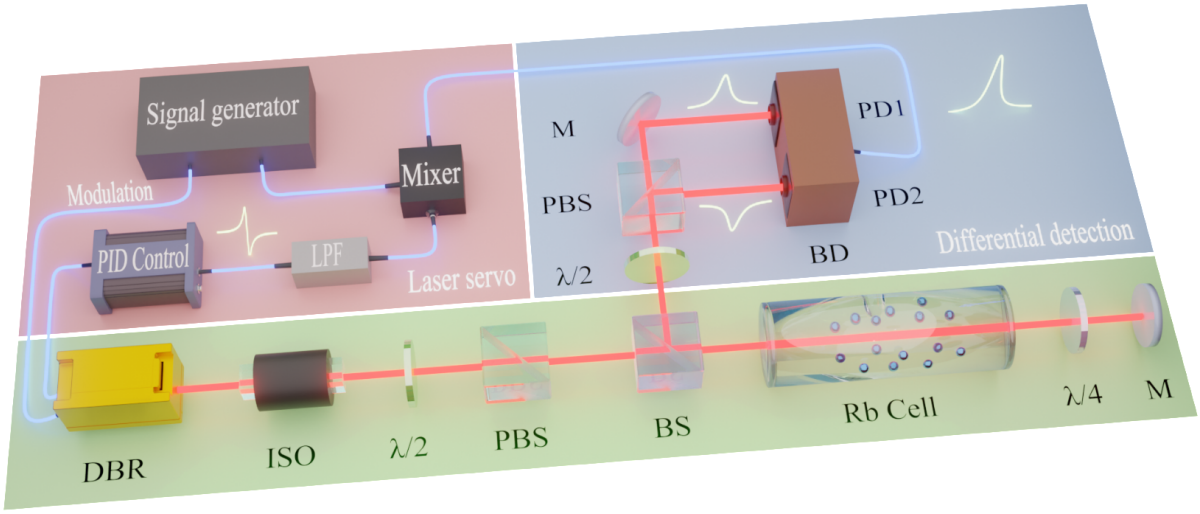


Figure 3. Schematic of the FDS-based vapor cell optical frequency reference. DBR: distributed Bragg reflector laser, $\lambda/2$: half-wave plate, ISO: isolator, BS: beam splitter, $\lambda/4$: quarter-wave plate, M: mirror, PBS: polarizing beam splitter, PD: photodiode, BD: balanced detector, LPF: low pass filter.

Full differential spectroscopy is implemented using the experimental setup depicted in Fig. 3. A distributed Bragg reflector laser (Photodigm, PH795DBR) pumps the Rb cell with a 1.5 mm collimated beam. The laser's intrinsic linewidth is narrowed to ~30 kHz through injection locking to a Fabry-Pérot (FP) cavity[47], and its frequency is tuned to the ^{87}Rb D_1 line by adjusting both the current and FP cavity length. A 30 dB optical isolator (ISO, Thorlabs, IO-5-780-VLP) is placed in the beam path to prevent optical feedback. The laser power P_L at the cell input is controlled using a half-wave plate followed by a polarization beam splitter (PBS). After passing through a beam splitter (BS), the transmitted beam propagates through an isotope-enriched ^{87}Rb cylindrical vapor cell (diameter 20 mm, length 50 mm). The cell temperature is maintained at approximately 30 °C, and is surrounded by a single layer of permalloy magnetic shielding to attenuate stray magnetic fields. Using a fluxgate magnetometer, the residual magnetic field inside the permalloy shield was measured to be lower than 0.3 μT.

Following interaction with the atomic vapor, the pump beam is reflected by a mirror, converted into a counter-propagating probe beam that overlaps spatially with the pump beam. To investigate probe beam polarization effects, a quarter-wave plate is inserted between the mirror and the vapor cell. This plate is mounted on a motorized rotation stage (Thorlabs, KPRM1E/M) for precise adjustment of the polarization angle θ. The transmitted probe beam is then spatially separated by the initial BS. To enhance the signal extraction from the reflected probe beam, the BS with a 10:90 (T: R) splitting ratio is employed. After

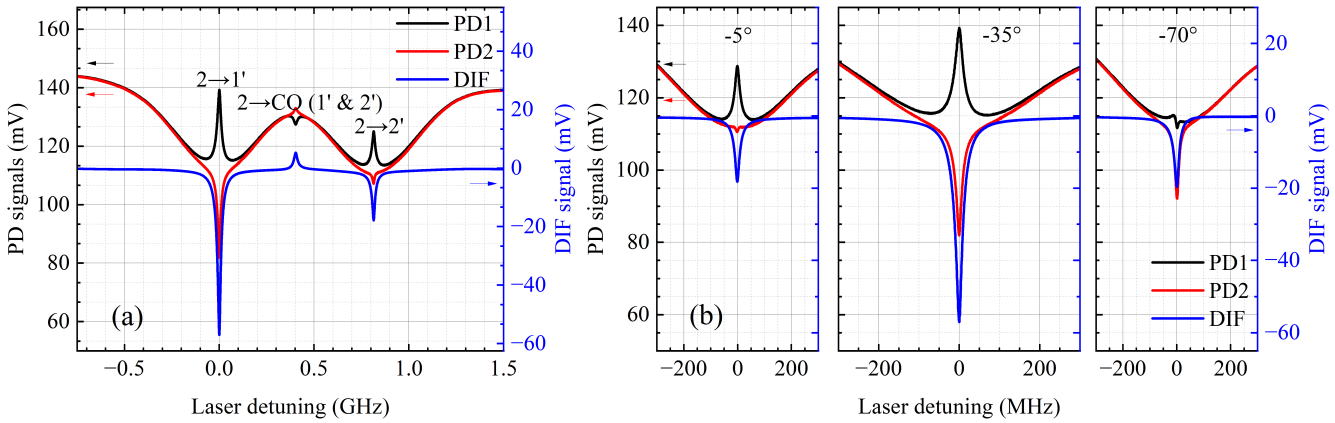


Figure 4. Experimentally measured FDS spectra. (a) Typical spectral signals in the D_1 line of ^{87}Rb at $P_L = 50\ \mu$W and $\theta = -35°$. 2, 1′ and 2′ stand for $|F = 2\rangle$, $|F' = 1\rangle$, $|F' = 2\rangle$, respectively. (b) Zoom of the FDS-based Doppler-free resonance ($|F = 2\rangle \rightarrow |F' = 1\rangle$ transition) for three values of the angle θ: $-5°$, $-35°$, and $-70°$.

spatial separation, the probe beam passes through another PBS, where its orthogonal polarization components are detected by a balanced photodetector (BPD, Thorlabs, PDB210A/M). A half-wave plate placed before this PBS balances these components, enabling EIT and EIA signal acquisition with the same background.

Results

Spectral characterization

Full differential spectroscopy results are presented in Fig. 4, showing the EIT, EIA, and DIF signals obtained by scanning the laser frequency detuning. The two peaks in Fig. 4(a) correspond to the resonance transitions of $|F = 2\rangle \rightarrow |F' = 1\rangle$ and $|F = 2\rangle \rightarrow |F' = 2\rangle$ of the ^{87}Rb D_1 line, with the intermediate peak representing the crossover resonance. Both EIT and EIA signals exhibit identical Doppler backgrounds, which are nearly eliminated through differentiation. This observation confirms the validity of the theoretical model and analysis presented in Fig. 2(a). Figure 4(b) displays the spectra for the $|F = 2\rangle \rightarrow |F' = 1\rangle$ transition at three specific angles. At $-5°$ and $-70°$, the observed spectra are similar to those obtained from conventional DSAS. In these cases, one detection port exhibits either an EIT or EIA signal, while the other port shows only Doppler-broadened background but no or weak Doppler-free signal, enabling common-mode noise rejection via differential detection[48]. In contrast, at the intermediate angle of $-35°$, the proposed FDS scheme simultaneously yields both EIT and EIA signals. This yields more effective common-mode noise suppression than conventional DSAS and doubled signal amplitude. Specifically, the measured signal amplitudes are -28.3 mV for EIT and 29.1 mV for EIA, corresponding to contrasts of -25.4% and 26.2%, respectively. Notably, the DIF signal reaches 57.4 mV, yielding a contrast of 51.7%, nearly twice the contrast observed for either individual EIT or EIA signal.

Features of the spectroscopic signal versus polarization angle

The figure of merit $M = S/\Delta\nu$, with $\Delta\nu$ the linewidth of the resonance, determines the short-term stability (σ_y at 1 s) of the frequency reference. Figures 5(a)-5(d) show the measured contrast, amplitude, linewidth, and M for the PD1, PD2, and DIF signals versus the polarization angle θ. Figure 5(a) shows that the contrast variation with θ closely aligns with theoretical predictions (see Fig. 2(b)). Slight discrepancies in absolute values between experimental and simulation data likely arise from model simplifications and optical component imperfections. Quantitatively, for the DIF signal, the absolute deviation between the theoretical and experimental contrast ranges from approximately 0.2 to 3.3 percentage points across the investigated polarization angle range. This level of agreement is excellent and validates the five-level model for the parameter regime investigated in this work. Figure 5(b) illustrates the dependence of the resonance amplitude on the polarization angle. Since the background becomes insensitive to the polarization angle after balancing the background using the half-wave plate, the dependence of the amplitude on the angle is similar to that of the contrast.

Figure 5(c) shows the evolution of the resonance linewidth $\Delta\nu$ with θ. The measured linewidth data follows the same trends as theoretical predictions from Fig. 2(c). Over the angular range of approximately $5° \leq |\theta| \leq 70°$, the DIF linewidth consistently lies between those of the EIT and EIA signals, as predicted with the model (see Fig. 2(c)). Near the extreme angles (5° and 70°), the theoretical model predicts sharper variations than observed experimentally. This deviation is not surprising. Indeed, in these regimes, the signal amplitude approaches zero and the resonance switches between EIT and EIA, making both the theoretical model (which relies on simplified decoherence parameters) and the experimental linewidth extraction (which

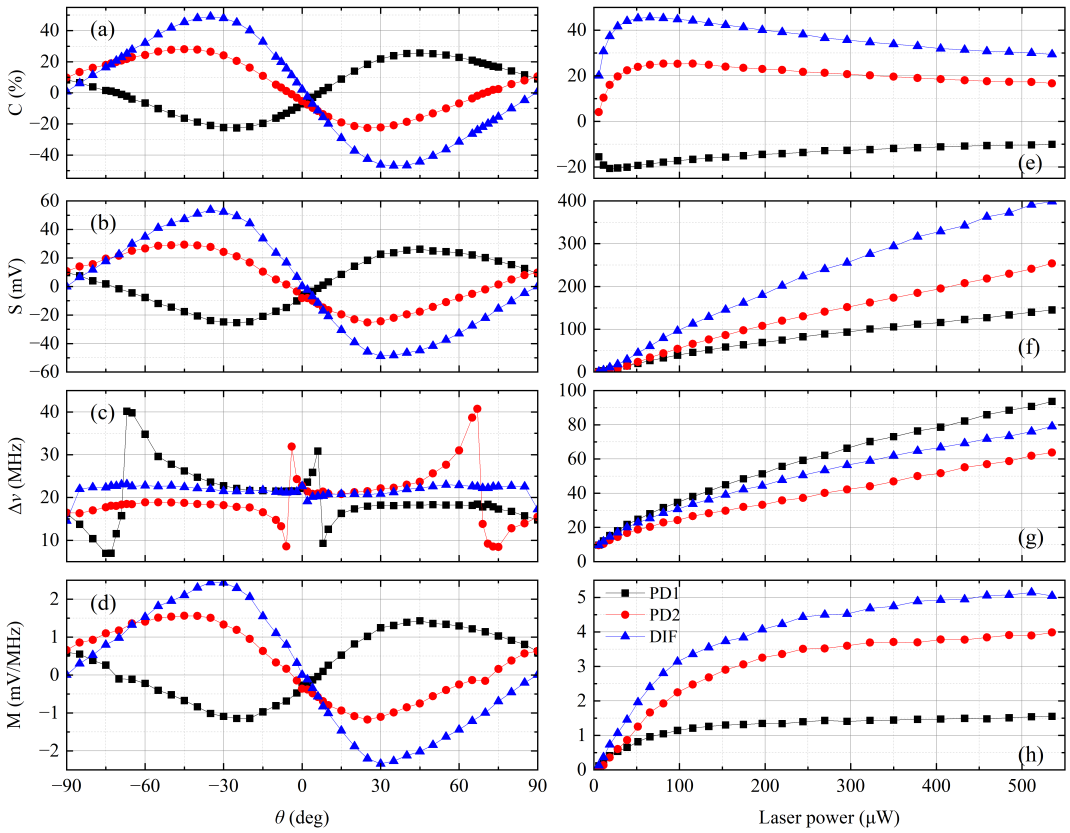


Figure 5. Spectral characterization of the FDS-based Doppler-free resonance versus polarization angle and laser power. (a-d) Contrast, amplitude, linewidth, and figure of merit versus polarization angle at $P_L = 50\ \mu$W. (e-h) These spectral characterization versus laser power at $\theta = -35°$.

becomes sensitive to noise and baseline fluctuations) less reliable. A numerical difference is observed between the calculated and measured linewidths throughout the measured range, which we attribute to the estimated rather than precisely calibrated values of the transit-time broadening γ_1 and the Zeeman coherence relaxation rate γ_2 in the analytical model. The dependence of M on the polarization angle θ is shown in Fig. 5(d). Despite linewidth discontinuities near $|\theta| = 5°$ and $70°$, M reaches its maximum around $|\theta| = 35°$. This angle was consequently selected for subsequent experiments unless otherwise specified.

Features of the spectroscopic signal versus laser power

We have also measured the features of the EIT, EIA, and DIF signals versus the incident laser power (Fig. 5(e)-5(h)). Figure 5(e) shows that the contrast of those signals increases rapidly below 50 μW before gradually decreasing at higher powers due to population leakage. This occurs because optical pumping between hyperfine levels gradually dominates over Zeeman-level pumping at elevated powers. Notably, the DIF signal achieves approximately twice the maximum contrast of individual EIT or EIA signals. The different power requirements for maximum contrast in EIT and EIA likely stem from distinct absorption mechanisms such as saturation. Figure 5(f) shows that the amplitude of EIT, EIA and DIF signals increases as the power increases. Figure 5(g) shows that linewidths exhibit power broadening. The DIF signal broadening lies between that of EIT and EIA throughout the measured range. Both experimental and theoretical linewidths (see Fig. 2(e)) show the same power-broadening trend, confirming again that the model correctly captures the underlying physics. Figure 5(h) demonstrates a significant enhancement of M at low powers due to the signal amplitude increasing more rapidly than the linewidth. However, it gradually saturates with increased laser power.

Features of the spectroscopic signal versus cell temperature and magnetic field

We have also measured the dependence of the sub-Doppler resonance features on the cell temperature and the static magnetic field. Corresponding results are reported and briefly discussed in Supplementary Note 2.

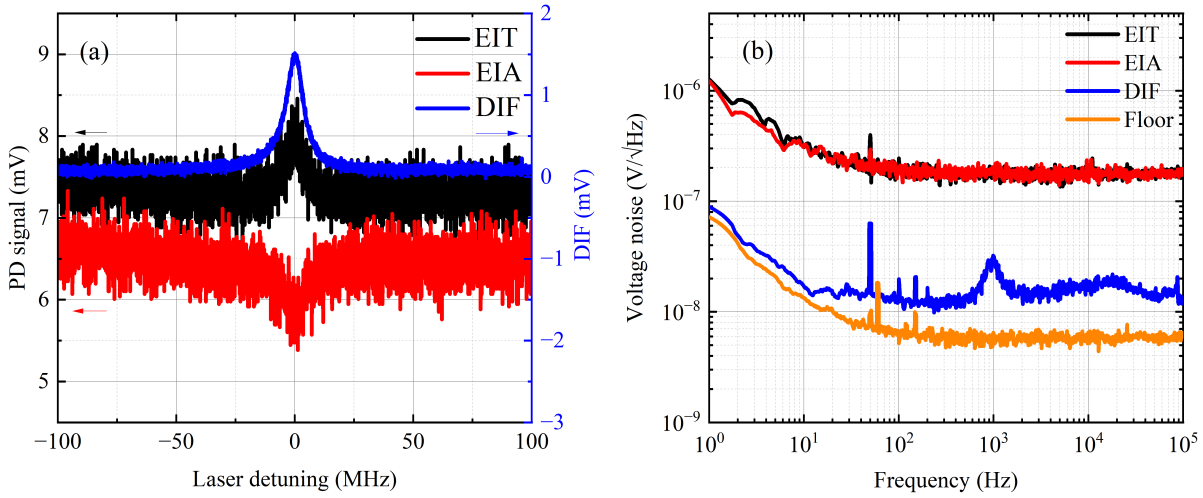


Figure 6. Low-power FDS signals and corresponding noise spectra. (a) EIT, EIA and DIF signals obtained at low power (the EIA signal is vertically offset for clarity). (b) Voltage noise spectra obtained for the signals shown in (a). The instrument noise floor is also shown for reference. Experimental parameters for both panels: $P_L = 5\ \mu$W, $\theta = -45\ ^\circ$.

Noise characterization

The primary advantage of FDS lies in the enhancement of the SNR. Key noise sources of the system include frequency modulation to amplitude modulation (FM-AM), amplitude modulation to amplitude modulation (AM-AM), intermodulation noise[49], shot noise and PD noise. Figure 6(a) shows the spectral signals at $P_L = 5\ \mu$W. At this very low power, the SNR of the signals detected at PD1 and PD2 outputs is very low. In contrast, the differential detection provides a resonance with a significantly enhanced SNR.

We quantitatively evaluate noise suppression using a dynamic signal analyzer (Stanford Research, SR785) to measure power spectral densities of each PD signal. Measurements are taken with the laser frequency tuned to the half-maximum of the Doppler-free resonance. With $P_L = 5\ \mu$W and $\theta = -45^\circ$ (Fig. 6(b)), the differential scheme exhibits significantly suppressed noise. In these conditions, EIT and EIA signals show a detection noise of $1.8 \times 10^{-7}\ \mathrm{V}/\sqrt{\mathrm{Hz}}$ at 100 kHz Fourier frequency, while the DIF signal shows a noise of $1.3 \times 10^{-8}\ \mathrm{V}/\sqrt{\mathrm{Hz}}$, i.e., more than tenfold reduction.

Noise suppression versus polarization

In cell-stabilized laser experiments, error signals for frequency locking are typically obtained via synchronous modulation-demodulation techniques, the applied modulation frequency being usually in the 10 kHz - 1 MHz range, where the detection noise and the contribution of the intermodulation effect[49] to the atomic reference frequency stability are reduced[50]. Therefore, to characterize noise suppression versus polarization angle, we analyzed the voltage noise of each PD signal at 100 kHz (bandwidth of SR785) Fourier frequency (Fig. 7(a)). Across all polarization angles, PD1 and PD2 noise vary little while the DIF noise is about 4 times smaller.

Figure 7(b) depicts the SNR dependence on the polarization angle θ. EIT and EIA maintain stable SNR $> 10^5$ except at $|\theta| \sim 5^\circ$ or 70° where the sign of the Doppler-free signal (S) is reversed. The FDS scheme achieves optimal SNR = 10^6 at $\theta = -35^\circ$, representing a tenfold improvement over conventional SAS (red -70° or black -5°), and a twofold enhancement versus single-beam DSAS (blue -70°).

Noise suppression versus laser power

We similarly examined laser power effects on the voltage noise of each PD signal at $\sim$ 100 kHz (Fig. 7(c)). PD1 and PD2 noise initially grow slowly with increasing power, whereas DIF noise demonstrates a pronounced initial rise. All three signals subsequently follow similar growth trends. Below 50 μW, DIF signals demonstrate superior noise suppression, though this advantage diminishes at higher powers. Figure 7(d) shows the SNR versus the pump power. DIF signals achieve significantly enhanced SNR compared to PD1/PD2, exceeding a tenfold improvement below 50 μW.

According to the noise model and analysis in Ref[31], the noise corresponding to PD1, PD2 and DIF signals can be expressed

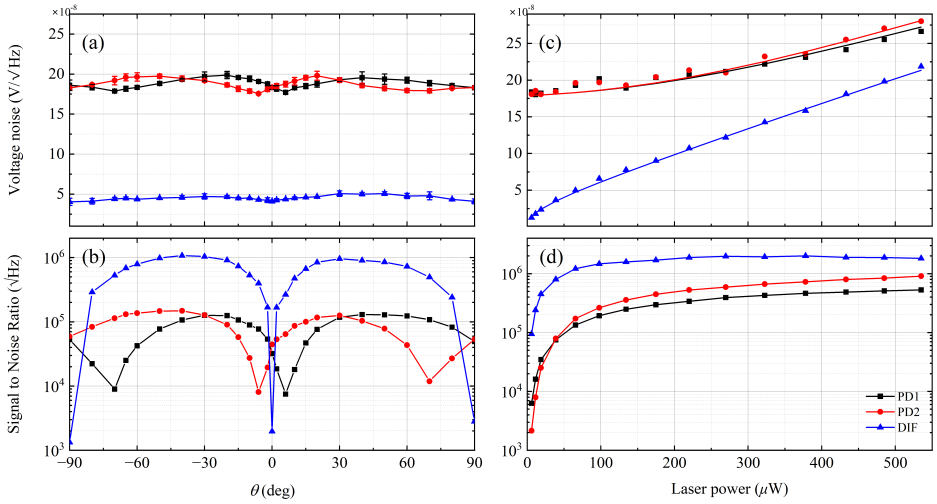


Figure 7. Voltage noise and SNR versus polarization angle and laser power. (a) Voltage noise at f = 100 kHz versus θ at $P_L = 50\ \mu$W. (b) SNR versus θ under the same conditions. (c) Voltage noise versus laser power at $\theta = -35°$. (d) SNR versus laser power. Error bars in (a), where visible, represent the standard deviation of the mean from n=3 repeated measurements.

as follows:

$$\begin{aligned} N_1 &= \left({N_{AM1}}^2 + {N_{P1}}^2 + {N_{SN}}^2\right)^{1/2} \\ N_2 &= \left({N_{AM2}}^2 + {N_{P2}}^2 + {N_{SN}}^2\right)^{1/2} \\ N_{DIF} &= \left((1-\alpha)^2\left({N_{AM1}}^2 + {N_{AM2}}^2\right) + {N_{P3}}^2 + 2{N_{SN}}^2\right)^{1/2} \end{aligned} \tag{3}$$

where N_{AM1} and N_{AM2} represent the AM-AM noise from EIT and EIA signals, respectively, which are power-dependent. FM-AM noise is ignored. N_{Pi}(i = 1, 2, 3) is the measured detector noise of the three ports (PD1, PD2, DIF) without incident light, which are 1.79×10^{-7} V/$\sqrt{\text{Hz}}$, 1.79×10^{-7} V/$\sqrt{\text{Hz}}$, and 7.84×10^{-9} V/$\sqrt{\text{Hz}}$, respectively. N_{SN} is the shot noise, that is $\sqrt{2eIG_R}$, where e is the electron charge, I the photocurrent, and G_R the transimpedance gain. α is a free parameter representing the noise rejection ratio.

Theoretical expectation (solid blue line, Fig. 7(c)) with α = 0.35 indicates 35% AM-AM noise suppression via FDS. To understand the behavior of the SNR versus the pump beam power, the SNR can be simply written as $S/(N_{AMi} + N_{Pi})$. At low power, minimal resonance amplitudes reduce the AM-AM noise contribution, making the detector noise dominant. Here, the DIF signal primarily enhances SNR by suppressing N_{Pi}. As the power increases, N_{AMi} gradually exceeds N_{Pi}, making AM-AM noise suppression the dominant advantage. This benefit diminishes at higher powers due to an increase in non-common-mode noise (e.g., FM-AM and shot noise).

Short-term stability of the optical frequency reference

The beatnote signal from two quasi-identical systems is measured for Allan deviation analysis. Each system uses a DBR laser which can be pre-stabilized through injection locking to a FP cavity. The resulting frequency stability of a single laser system, obtained by dividing the Allan deviation of the beatnote by $\sqrt{2}$, is reported in Fig. 8 for three different configurations (free-running, injection-locked to the FP-cavity but not locked to the atoms, pre-stabilized to the FP-cavity + locked to the atoms using FDS, i.e. dual-locked).

In the free-running regime, the laser stability is 1.4×10^{-9} at 1 s and then degrades, reaching 10^{-8} at 100 s. With injection locking to the FP cavity, the laser stability is improved at the level of 1.4×10^{-10} at 1 s and 7×10^{-9} at 100 s. By stabilizing the laser both to the FP cavity and to the atomic cell using the FDS scheme, the laser stability is significantly improved by about 3 orders of magnitude, yielding a level of 1.2×10^{-13} at 1 s, and remaining below the 10^{-12} level up to 1000 s. This measured short-term stability at 1 s, one order of magnitude better than the one reported in our previous work[33], is in agreement with the predicted stability (1.3×10^{-13}) extracted from the laser phase noise spectra reported in Supplementary Note 3.

Supplementary Table 1 summarizes the contributions of the main noise sources to the optical reference short-term stability budget. It shows that the main contribution to the cell-stabilized laser stability at 1 s is the laser FM-AM noise process, at the level of 4.9×10^{-14}, followed by the photon shot noise (3.8×10^{-14}). This budget suggests that an improved stability result might be obtained using a laser with lower frequency noise.

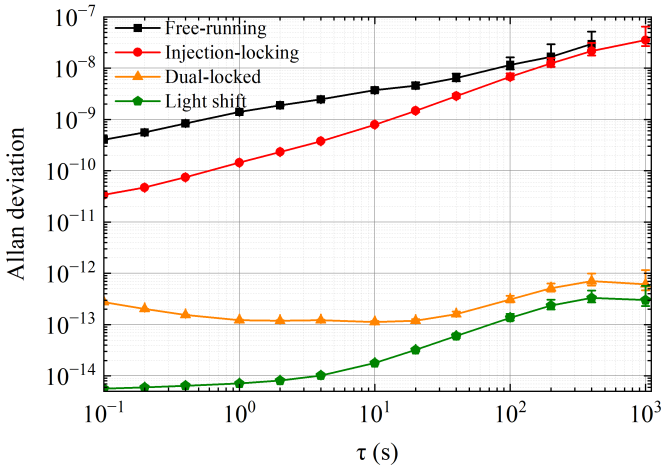


Figure 8. Allan deviation of a single laser under three conditions. Free-running, injection-locked to the FP cavity, and injection-locked to the FP cavity + FDS-based stabilization to the Rb cell ("Dual-locked"). Experimental parameters are: P_L = 50 μW, $\theta = -35$ °. The contribution of laser power fluctuations on the short-term stability is shown for information. Error bars represent the standard deviation of the mean from n frequency samples at each integration time τ. For $\tau = 1$ s, the number of samples n=2000.

For integration times higher than 10 s, the stability of the FDS-stabilized laser might be limited by several environmental factors, such as laser power fluctuations (which induce AC Stark shifts), cell temperature and magnetic field variations, temperature variations of optical components (the waveplates, beam splitters, etc), or the photocurrent imbalance drift in the balanced detector. As shown in Fig. 8, laser power fluctuations are evaluated to date as a major limiting factor to the reference stability after a few tens of seconds. Future studies will aim to evaluate these respective contributions and to implement techniques for their mitigation, including active laser power stabilization, improved temperature control of the optical components, or implementation of auto-balancing detection schemes[51–56].

Conclusion

This study reports full differential spectroscopy (FDS) in a vapor cell. This method, through the manipulation of coherent dark states using monochromatic light and a single beam configuration, enables the simultaneous detection of EIT and EIA resonances superimposed on the same Doppler-broadened background. Via differential detection, a spectroscopic signal with doubled resonance amplitude and reduced background and noise is obtained. We characterize in detail the impact of the relative polarization angle (between the two counterpropagating beams) and the laser power on the amplitude, contrast, linewidth and noise of the FDS-based Doppler-free resonance. We demonstrate a DBR laser, pre-stabilized to a Fabry-Pérot cavity through injection locking (for intrinsic FM noise reduction), locked to a Rb vapor cell using FDS with a fractional frequency stability of 1.2×10^{-13} at 1 s and below 10^{-12} at 1000 s. The short-term stability at 1 s, that remains limited by the laser FM-AM conversion process, demonstrates the potential of the FDS approach for the development of simple-architecture and high-stability vapor cell optical frequency references. The FDS technique may also be attractive for coherent atom-light manipulation experiments, quantum sensors and high-resolution spectroscopy.

References

1. Safronova, M. S. *et al.* Search for new physics with atoms and molecules. *Rev. Mod. Phys.* **90**, 025008, DOI: 10.1103/RevModPhys.90.025008 (2018).
2. Degen, C. L., Reinhard, F. & Cappellaro, P. Quantum sensing. *Rev. Mod. Phys.* **89**, 035002, DOI: 10.1103/RevModPhys.89.035002 (2017).
3. Conroy, R. Frequency standards, metrology and fundamental constants. *Contemp. Phys.* **44**, 99–135, DOI: 10.1080/00107910210164020 (2003).
4. Roslund, J. D. *et al.* Optical clocks at sea. *Nature* **628**, 736–740, DOI: 10.1038/s41586-024-07225-2 (2024).
5. Hilton, A. P. *et al.* Demonstration of a mobile optical clock ensemble at sea. *Nat. Commun.* **16**, 6063, DOI: 10.1038/s41467-025-61140-2 (2025).

6. Pappas, P., Burns, M., Hinshelwood, D., Feld, M. & Murnick, D. Saturation spectroscopy with laser optical-pumping in atomic barium. *Phys. Rev. A* **21**, 1955–1968, DOI: 10.1103/PhysRevA.21.1955 (1980).

7. Rovera, G. D., Santarelli, G. & Clairon, A. A laser diode system stabilized on the caesium D_2 line. *Rev. Sci. Instrum.* **65**, 1502–1505, DOI: 10.1063/1.1144882 (1994).

8. Affolderbach, C. & Mileti, G. Tuneable, stabilised diode lasers for compact atomic frequency standards and precision wavelength references. *Opt. Lasers Eng.* **43**, 291–302, DOI: 10.1016/j.optlaseng.2004.02.009 (2005).

9. Liu, X. & Boudot, R. A distributed-feedback diode laser frequency stabilized on Doppler-free Cs D_1 line. *IEEE Transactions on Instrumentation Meas.* **61**, 2852–2855, DOI: 10.1109/TIM.2012.2196399 (2012).

10. Hummon, M. T. *et al.* Photonic chip for laser stabilization to an atomic vapor with 10^{-11} instability. *Optica* **5**, 443–449, DOI: 10.1364/OPTICA.5.000443 (2018).

11. Strangfeld, A. *et al.* Prototype of a compact rubidium-based optical frequency reference for operation on nanosatellites. *J. Opt. Soc. Am. B* **38**, 1885, DOI: 10.1364/josab.420875 (2021).

12. Strangfeld, A., Wiegand, B., Kluge, J., Schoch, M. & Krutzik, M. Compact plug and play optical frequency reference device based on doppler-free spectroscopy of rubidium vapor. *Opt. Express* **30**, 12039–12047, DOI: 10.1364/OE.453942 (2022).

13. Utreja, S., Rathore, H., Das, M. & Panja, S. Frequency stabilization of multiple lasers to a reference atomic transition of Rb. *Sci. Rep.* **12**, 20624, DOI: 10.1038/s41598-022-24952-6 (2022).

14. Zhang, A. *et al.* Exploration of a vapor cell optical frequency standard scheme implemented using Doppler-free spectroscopy. *Opt. Lett.* **49**, 5475–5478, DOI: 10.1364/OL.534239 (2024).

15. Klinger, E. *et al.* Cs microcell optical reference at 459 nm with short-term frequency stability below 2×10^{-13}. *Appl. Phys. Lett.* **126**, 124003, DOI: 10.1063/5.0261771 (2025).

16. Schmidt, O., Knaak, K., Wynands, R. & Meschede, D. Cesium saturation spectroscopy revisited: How to reverse peaks and observe narrow resonances. *Appl. Phys. B-Lasers Opt.* **59**, 167–178, DOI: 10.1007/BF01081167 (1994).

17. Yang, D. & Wang, Y. Study on the saturation absorption of cesium. *Opt. Commun.* **74**, 54–58, DOI: 10.1016/0030-4018(89)90489-6 (1989).

18. Preston, D. Doppler-free saturated absorption: Laser spectroscopy. *Am. J. Phys.* **64**, 1432–1436, DOI: 10.1119/1.18457 (1996).

19. Hänsch, T., Shanin, I. & Schawlow, A. High-resolution saturation spectroscopy of the sodium D lines with a pulsed tunable dye laser. *Phys. Rev. Lett.* **27**, 707–710, DOI: 10.1103/PhysRevLett.27.707 (1971).

20. Camparo, J. & Coffer, J. Conversion of laser phase noise to amplitude noise in a resonant atomic vapor: The role of laser linewidth. *Phys. Rev. A* **59**, 728–735, DOI: 10.1103/PhysRevA.59.728 (1999).

21. Mielenz, K. D. Beam-splitter and cell-window errors in fluorescence spectrometry. *Appl. Opt.* **18**, 4134–4137, DOI: 10.1364/AO.18.004134 (1979).

22. Kitching, J. Chip-scale atomic devices. *Appl. Phys. Rev.* **5**, 031302, DOI: 10.1063/1.5026238 (2018).

23. Wieman, C. & Hansch, T. Doppler-free laser polarization spectroscopy. *Phys. Rev. Lett.* **36**, 1170–1173, DOI: 10.1103/PhysRevLett.36.1170 (1976).

24. Pearman, C. *et al.* Polarization spectroscopy of a closed atomic transition: applications to laser frequency locking. *J. Phys. B: At. Mol. Opt. Phys.* **35**, 5141–5151, DOI: 10.1088/0953-4075/35/24/315 (2002).

25. Torrance, J. S., Sparkes, B. M., Turner, L. D. & Scholten, R. E. Sub-kilohertz laser linewidth narrowing using polarization spectroscopy. *Opt. Express* **24**, 1396–1406, DOI: 10.1364/OE.24.011396 (2016).

26. Brumfield, B. & Wysocki, G. Faraday rotation spectroscopy based on permanent magnets for sensitive detection of oxygen at atmospheric conditions. *Opt. Express* **20**, 29727–29742, DOI: 10.1364/OE.20.029727 (2012).

27. Li, J. *et al.* Shot-noise-limited optical Faraday polarimetry with enhanced laser noise cancelling. *J. Appl. Phys.* **115**, 103101, DOI: 10.1063/1.4867743 (2014).

28. Quan, W. *et al.* Far off-resonance laser frequency stabilization using multipass cells in Faraday rotation spectroscopy. *Appl. Opt.* **55**, 2503–2507, DOI: 10.1364/AO.55.002503 (2016).

29. Groswasser, D. *et al.* Retroreflecting polarization spectroscopy enabling miniaturization. *Rev. Sci. Instruments* **80**, 093103, DOI: 10.1063/1.3213076 (2009).

30. Kunz, P. D., Heavner, T. P. & Jefferts, S. R. Polarization-enhanced absorption spectroscopy for laser stabilization. *Appl. Opt.* **52**, 8048–8053, DOI: 10.1364/AO.52.008048 (2013).

31. Li, Q. *et al.* Noise suppression by differential detection of simultaneous electromagnetically induced transparency and absorption in counterpropagating bichromatic light. *New J. Phys.* **25**, 103039, DOI: 10.1088/1367-2630/ad01d1 (2023).

32. Yun, P., Boudot, R. & de Clercq, E. Coherent population trapping with high common-mode noise rejection using differential detection of simultaneous dark and bright resonances. *Phys. Rev. Appl.* **19**, 024012, DOI: 10.1103/PhysRevApplied.19.024012 (2023).

33. Yun, P., Boudot, R., Hao, Q. & Zhang, S. Enhanced absorption in Doppler-free spectroscopy of the Rb atom D_1 line with monochromatic light: Application to laser-frequency stabilization. *Phys. Rev. Appl.* **23**, 034063, DOI: 10.1103/PhysRevApplied.23.034063 (2025).

34. Tsygankov, E. *et al.* Single-frequency inverted Doppler-free resonance as a platform for chip-scale optical clock. *arXiv:2505.02219v1* DOI: 10.48550/arXiv.2505.02219 (2025).

35. Hafiz, M. A., Coget, G., Clercq, E. D. & Boudot, R. Doppler-free spectroscopy on the Cs D_1 line with a dual-frequency laser. *Opt. Lett.* **41**, 2982–2985, DOI: 10.1364/OL.41.002982 (2016).

36. Gusching, A. *et al.* Short-term stability of Cs microcell-stabilized lasers using dual-frequency sub-Doppler spectroscopy. *J. Opt. Soc. Am. B* **38**, 3254–3260, DOI: 10.1364/JOSAB.438111 (2021).

37. Hodby, E., Donley, E. A. & Kitching, J. Differential atomic magnetometry based on a diverging laser beam. *Appl. Phys. Lett.* **91**, 011109, DOI: 10.1063/1.2753763 (2007).

38. Ichihara, S., Mizutani, N., Ito, Y. & Kobayashi, T. Differential measurement with the balanced response of optically pumped atomic magnetometers. *IEEE Transactions on Magn.* **52**, 1–9, DOI: 10.1109/TMAG.2016.2547364 (2016).

39. Yuan, J., Du, P., Yang, F., Quan, W. & Li, J. Simultaneous improvement of the sensitivity and resolution of CPT magnetometers based on phase delay and differential method. *Opt. Lett.* **49**, 3858–3861, DOI: 10.1364/OL.528628 (2024).

40. Zheng, J. Differential birefringent fiber frequency-modulated continuous-wave sagnac gyroscope. *IEEE Photonics Technol. Lett.* **17**, 1498–1500, DOI: 10.1109/LPT.2005.848559 (2005).

41. ChunXi, Z. *et al.* Reduction of nonreciprocal errors in a differential interferometric fiber optical gyroscope using optically differential processing. *Sci. China Technol. Sci.* **57**, 1631–1635, DOI: 10.1007/s11431-014-5599-9 (2014).

42. Yang, Y., Li, S., Yang, F. & Jin, W. Differential fiber optic gyroscope driven by two broadband sources of different wavelengths. *IEEE Access* **8**, 65443–65449, DOI: 10.1109/ACCESS.2020.2984006 (2020).

43. Boyd, R. W. & Gauthier, D. J. Controlling the velocity of light pulses. *Science* **326**, 1074–1077, DOI: 10.1126/science.1170885 (2009).

44. Ouyang, H. *et al.* Polarization-tunable nonlinear absorption patterns from saturated absorption to reverse saturated absorption in anisotropic ges flake and an application of all-optical switching. *Sci. China Mater.* **63**, 1489–1502, DOI: 10.1007/s40843-020-1289-7 (2020).

45. Davis, W. O. C. *et al.* Fast, low-loss, all-optical phase modulation in warm rubidium vapour. *Quantum Sci. Technol.* **10**, 025001, DOI: 10.1088/2058-9565/ad9fa3 (2025).

46. Demtröder, W. *Laser spectroscopy 1: basic principles* (Springer, 2014).

47. Liang, W. & Liu, Y. Compact sub-hertz linewidth laser enabled by self-injection lock to a sub-milliliter FP cavity. *Opt. Lett.* **48**, 1323–1326, DOI: 10.1364/OL.481552 (2023).

48. Wang, B., Peng, X., Wang, H., Liu, Y. & Guo, H. Laser-frequency stabilization with differential single-beam saturated absorption spectroscopy of ^{4}He atoms. *Rev. Sci. Instrum.* **93**, 043001, DOI: 10.1063/5.0084605 (2022).

49. Audoin, C., Candelier, V. & Dimarcq, N. A limit to the frequency stability of passive frequency standards due to an intermodulation effect. *IEEE Transactions on Instrumentation Meas.* **40**, 121–125, DOI: 10.1109/TIM.1990.1032896 (1991).

50. Newman, Z. L. *et al.* High-performance, compact optical standard. *Opt. Lett.* **46**, 4702–4705, DOI: 10.1364/OL.435603 (2021).

51. Hobbs, P. C. D. Ultrasensitive laser measurements without tears. *Appl. Opt.* **36**, 903–920, DOI: 10.1364/AO.36.000903 (1997).

52. Hobbs, P. C. D. Shot-noise-limited optical measurements at baseband with noisy lasers. In *Laser Noise*, vol. 1376, 216–221, DOI: 10.1117/12.25014 (SPIE, 1991).

53. Halahovets, Y. *et al.* Scanning magneto-optical Kerr microscope with auto-balanced detection scheme. *Rev. Sci. Instrum.* **82**, 083706, DOI: 10.1063/1.3625687 (2011).

54. Jian-Qiang, L., Xu-Yang, W., Zeng-Liang, B. & Yong-Min, L. High precision auto-balance of the time-domain pulsed homodyne detector. *Acta Phys. Sinica* **65**, 100303, DOI: 10.7498/aps.65.100303 (2016).

55. Chang, C.-Y., Wang, L., Shy, J.-T., Lin, C.-E. & Chou, C. Sensitive Faraday rotation measurement with auto-balanced photodetection. *Rev. Sci. Instrum.* **82**, 063112, DOI: 10.1063/1.3602927 (2011).

56. Jo, J., Kim, Y., Hwangbo, C. K. & Kim, K. Sensitive measurement of the magneto-optic effect in the near infrared wavelength region with weak alternating magnetic fields. *Opt. Mater. Express* **8**, 2636–2642, DOI: 10.1364/OME.8.002636 (2018).

Funding

National Key R&D Program of China (2023YFC2205400); National Natural Science Foundation of China (Grant No. 12673083, Grant No. 12173043, Grant No. U1731132); CAS Project for Young Scientists in Basic Research (YSBR-69); Major Project of Scientific and Technological Innovation 2030 (2023ZD0301500).

Acknowledgements

We gratefully acknowledge Ms. Candy Xiong (NTSC) for thoroughly reading and polishing our manuscript.

Author contributions

Tenghui Yang: Experimental realization (lead); Data curation (lead); Formal analysis (lead); Writing-original draft (lead). Peter Yun: Conceptualization (lead); Theoretical model development (lead); Methodology (lead); Validation (lead); Writing-Reviewing and Editing (lead); Resources (lead). Rodolphe Boudot: Writing-Reviewing and Editing (lead). Qiang Hao: Writing- Reviewing and Editing (supporting). Wei Liang: Narrow linewidth laser implementation (lead). Shougang Zhang: Resources (supporting).

Competing interests

The authors declare no conflicts of interest.

Data availability

The datasets generated and analysed during the current study are available from the corresponding author on reasonable request.